



OPEN

Graphene on Mica - Intercalated Water Trapped for Life

SUBJECT AREAS:

ELECTRONIC PROPERTIES
AND DEVICES

GRAPHENE

O. Ochedowski, B. Kleine Bussmann & M. Schleberger

Fakultät für Physik and CENIDE, Universität Duisburg-Essen, 47048 Duisburg, Germany.

Received

19 May 2014

Accepted

22 July 2014

Published

18 August 2014

Correspondence and
requests for materials
should be addressed to
M.S. (marika.
schleberger@uni-due.
de)

In this work we study the effect of thermal processing of exfoliated graphene on mica with respect to changes in graphene morphology and surface potential. Mild annealing to temperatures of about 200 °C leads to the removal of small amounts of intercalated water at graphene edges. By heating to 600 °C the areas without intercalated water are substantially increased enabling a quantification of the charge transfer properties of the water layer by locally resolved Kelvin probe force microscopy data. A complete removal on a global scale cannot be achieved because mica begins to decompose at temperatures above 600 °C. By correlating Kelvin probe force microscopy and Raman spectroscopy maps we find a transition from *p*-type to *n*-type doping of graphene during thermal processing which is driven by the dehydration of the mica substrate and an accumulation of defects in the graphene sheet.

Because of its exceptional properties, graphene, an atomically thin layer of carbon atoms in sp^2 configuration, has attracted great interest in the scientific community. Especially its extremely high thermal and electronic conductivities, mechanical strength and impermeability to even the smallest gaseous molecules make graphene a highly interesting material for applications in e.g. electronics, photovoltaics, sensors and water desalination to name only a few^{1–8}.

Being a material which is nothing but surface, graphene is known to be largely influenced by the underlying substrate and the environment. Pure graphene should have no intrinsic charge carriers but in practice it often shows *p*-type doping caused by a combination of air humidity and oxygen molecules^{9–12}. Excess charge carriers (electrons as well as holes^{13–15}) can also be transferred from the substrate, which thus plays a major role for the performance of graphene devices. In addition, charge puddles and impurities in the substrate may act as efficient scattering sites, as observed for graphene on SiO_2 ^{16,17}. It is therefore of utmost importance to choose the substrate carefully and to quantify its specific doping and charge transfer properties. One of the most promising substrate candidates for future graphene devices is mica¹⁸. Using molecular beam epitaxy it has been shown that it is possible to directly grow graphene on mica¹⁹, which is an important factor for industrial applications. Mica is a layered silicate material that exhibits a very flat surface after cleavage. As a consequence, exfoliated graphene is also extremely flat with a root mean square (rms) of $\delta = 24.1 \text{ pm}^{20}$ measured by atomic force microscopy (AFM). However, this flatness can only be achieved by exfoliating graphene in a dry atmosphere. Exfoliation in ambient leads to intercalation of water layers^{21–27} which could prove detrimental for electronic devices. Raman spectroscopy, Kelvin probe force microscopy (KPFM) and scanning tunneling spectroscopy performed in ambient revealed a *p*-type doping from the substrate, that is effectively blocked by the intercalated water layers. It was suggested in ref. 24 to actually use water to modulate the electronic properties of graphene, but in practice controlling water islands locally would be extremely difficult to realize. Therefore one is confronted with the problem to remove the intercalated water.

In this work, high temperature processing in ultra high vacuum (UHV) of graphene on muscovite mica has been performed in order to study the effect of heating on the interfacial water layer. To this end, pristine and thermally processed samples have been thoroughly investigated with respect to morphology and work function. We present data from in situ non-contact AFM, showing that basically a complete removal of water cannot be achieved because decomposition of the mica substrate limits the maximum temperature. We therefore proceed by recording changes of the doping level of graphene due to in situ heating with locally resolved KPFM to probe the effect of intercalated water on the charge transfer between graphene and its substrate. This data is complemented by Raman spectroscopy measurements, indicating a clear correlation between thermally induced structural changes and changes in charge carrier concentration.

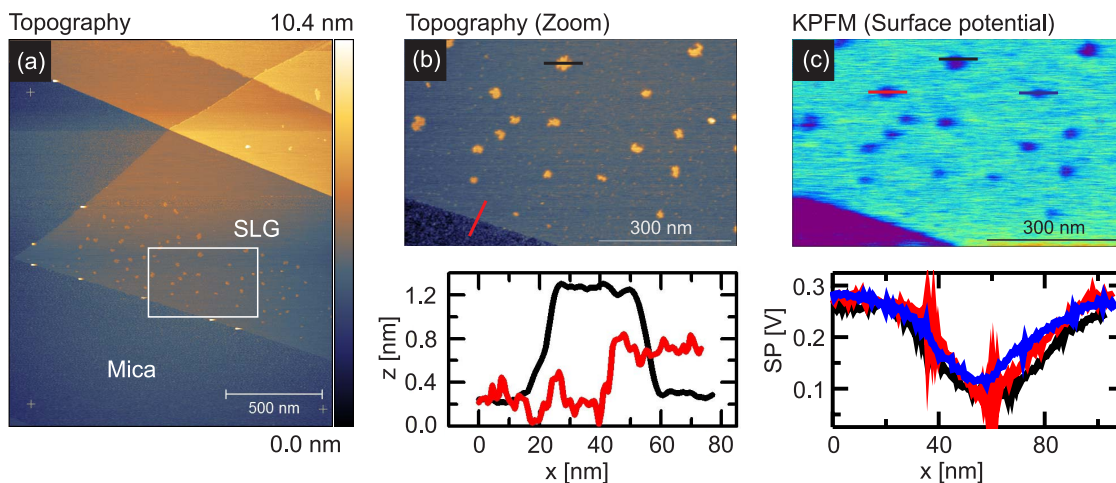


Figure 1 | (a) Non-contact AFM topography of a pristine graphene flake on mica. The SLG flake is decorated with water islands. (b) Zoom-in on the white box marked in (a). The red line profile denotes the height of the SLG flake on mica while the black line profile denotes the height of a water island. (c) Surface potential map corresponding to the topography in (b). Water islands lead to a decrease in surface potential by up to 200 mV.

Results

For our studies we used mechanically exfoliated graphene flakes supported on muscovite mica. In fig. 1(a) a non-contact AFM topography of a typical graphene flake on mica after introduction to UHV conditions ($p_{\text{base}} = 1 \times 10^{-10}$ mbar) is shown. The zoom-in topography image in (b) shows that the single layer graphene (SLG) flake is decorated with small islands. The red line profile in fig. 1(b) denotes the height of the SLG on mica which is about 0.4 nm. While this value corresponds well to the nominal interlayer spacing of graphite, we observe that the measured heights frequently vary between 0.4 nm and 0.9 nm. This is in agreement with values reported for SLG on mica varying between -0.8 nm and 1.0 nm^{19,24}. By exfoliating graphene on mica in ambient conditions, water layers will be trapped at the interface between graphene and mica which results in increased step heights measured by AFM^{22,28}. These interfacial water layers, IWL called in the following, have been found in different thicknesses from one to three IWL. The small islands which are up to 1.2 nm in height (see black line profile in fig. 1(b)) are attributed to water on top of graphene, as they can be easily removed by mild heating to 180°C, which is significantly below the temperature needed to clean graphene from contaminations^{52,53}. They can easily be identified in the surface potential map as well (see figure fig. 1(c)). Here, the water islands decrease the surface potential of graphene by up to 200 meV.

To obtain quantitative data from our KPFM measurements, the work function of the AFM tip is calibrated on few layer graphene areas on the sample. The work function value of graphite can be assigned to few layer graphene areas where the surface potential depends on the layer number²⁹. This procedure yields $\Phi_{\text{FLG}} = \Phi_{\text{Graphite}} = 4.65$ eV for few layer graphene (FLG). With the tip calibrated in this way, the work function of single- and bilayer graphene can be calculated using the relation $\Phi_{nG} = \Phi_{\text{Graphite}} + e(\text{CPD}_{\text{FLG}} - \text{CPD}_{nG})$, whereas CPD is the contact potential difference measured by KPFM between the AFM tip and the sample. In graphene, a variation of the work function is directly correlated to a shift of the Fermi energy ΔE_F with respect to the Dirac point³⁰. Based on the fact that the work function of graphene is around 4.57 eV^{31,32}, a work function higher than this value can be attributed to *p*-type doping and vice versa *n*-type doping for a lower work function.

Next we tried to apply a thermal treatment to remove the intercalated water film. To this end, several heating steps were performed at different temperatures and exposure times. The pristine SLG flake in fig. 2(a) with the continuous IWL exhibits a work

function of 4.83 eV which is lowered to 4.66 eV in areas where water islands are adsorbed on top of it as seen in fig. 1(c). Heating this sample to about 180°C for 1 hour can be used to remove the adsorbed water islands but not the interfacial water as can be seen in fig. 2(b). As the intercalated water cannot penetrate the graphene sheet, only small areas at the edge of graphene are freed from water. Because grain boundaries and defect sites are very rare in exfoliated graphene sheets, no effective alternative desorption pathways exist. The work function map shows a similar work function distribution, the work function is decreasing with increasing layer number. However, the work function of graphene in direct contact with mica is about 0.17 eV higher compared to graphene lying on the interfacial water layer. This is an important finding as it suggests that pristine graphene and mildly heated graphene both show *p*-type doping. In contrast to KPFM measurements in ambient (where *p*-type doping is always present because of humidity), this can be taken as proof that graphene on mica is indeed *p*-type doped by a charge transfer from the mica substrate.

The last images in fig. 2 show results that were obtained after heating the sample to about 600°C for 19 hrs. The area where the intercalated water layer has been removed has increased (dark blue areas in fig. 2(c)) but in large areas of the graphene flake intercalated water can still be clearly seen (light blue areas in fig. 2(c)). The work function has changed significantly over the whole flake: From 4.8 eV (greenish area in fig. 2(b)) to 3.93 eV (bluish area in fig. 2(c)) where the water has been removed, and from 4.65 eV to 4.28 eV in the areas where the water could not be removed. In addition, new characteristic features have appeared (marked with “nanoblisters” in fig. 2) with typical diameters of about 10 nm and heights of 0.3 to 1.5 nm. Note that these features are quite different from the water islands found before heating (fig. 1), because they are much higher and are located underneath the graphene and not on top of the graphene sheet. We repeated the experiment with other flakes and found that the observed changes are indeed characteristic but with small deviations with respect to absolute values (see fig. 4 for example).

At this point we want to stress that the observed change in work function upon excessive heating is not only surprisingly pronounced, it also represents a transition from *p*- to *n*-type doped graphene. Such a transition has never been observed for graphene on mica. Of course, any KPFM data has in general to be treated with great care due to uncertainties with respect to calibration. Therefore, to ensure that the work function values measured here are indeed correct, we undertook extra efforts to exclude the possibility that our calibration

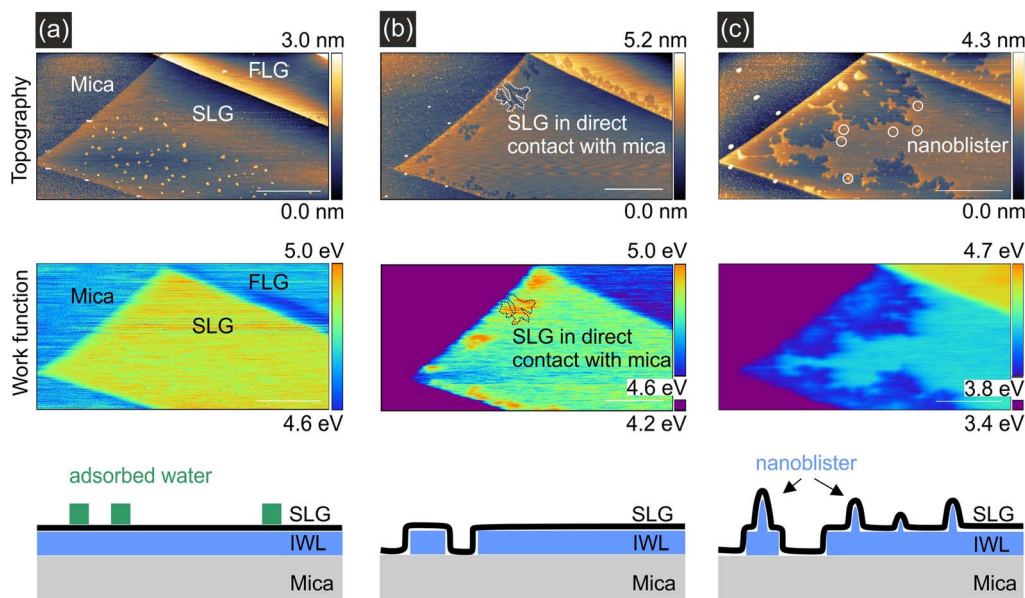


Figure 2 | (a) Topography and work function map of pristine graphene on mica. The work function decreases with increasing layer thickness. The sketch illustrates that a continuous IWL is beneath graphene while adsorbed water islands are on top of it. (b) Topography and work function map after heating the sample to 180°C for 1 hour. The water islands on graphene are removed and the IWL is not completely continuous anymore and graphene is partly in direct contact with the substrate. The work function is still decreasing with increasing layer thickness. (c) Topography and work function map after heating the sample to 600°C for 19 hours. The size of the IWL is further decreased and nanoblister beneath the SLG flake are formed. The contrast in the work function map is inverted, as the work function is now increasing with layer thickness (Scale bars in all images are 400 nm.)

material, few layer graphene, is affected by residual water (see suppl. material). Having excluded artifacts due to calibration, we must attribute the observed transition to heating-induced changes.

To test whether the original state of the system with respect to work function can be restored, we exposed a sample to ambient conditions for three days after it had undergone the same treatment

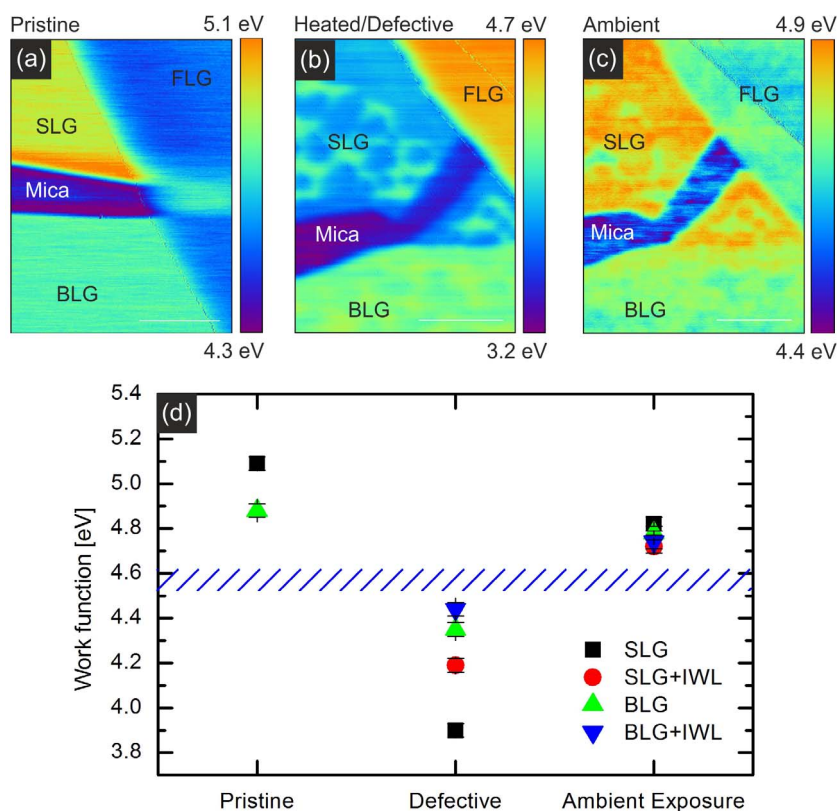


Figure 3 | (a) Work function map of a pristine mica supported SLG, BLG and FLG flake. The work function decreases with increasing layer thickness. (b) After heating to 600°C the work function is inverted and intercalated water causes an additional work function contrast on SLG and BLG. (c) Work function map after three days of exposure to ambient conditions. The work function is again inverted, restoring the work function similar to its pristine condition. (d) Summary of the work function measurements from (a–c) (Scale bars in all images are 400 nm.)

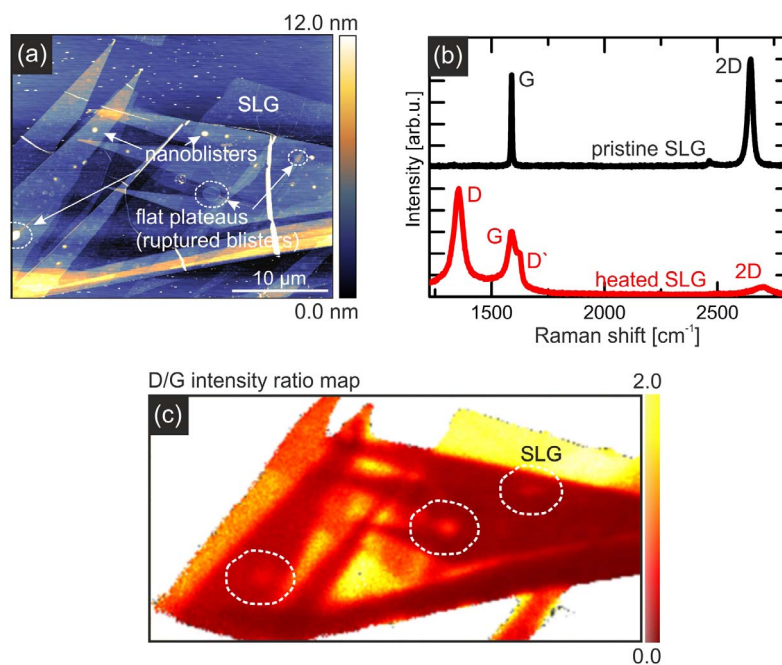


Figure 4 | (a) AFM topography of a graphene flake after in situ heat treatment. Nanoblister and areas with flat plateaus (ruptured nanoblister) are marked in the image. (b) Raman spectra of pristine and heat treated single layer graphene on mica. (c) Raman mapping of the D/G peak intensity ratio of the graphene flake shown in (a).

as described above. The results of this experiment are summarized in fig. 3. The work function of SLG in its pristine condition 5.09 eV (*p*-type) decreases to 3.90 eV (*n*-type) after in situ heat processing. The same transition can be observed for bilayer graphene (BLG) where the work function is decreasing from 4.88 eV to 4.35 eV. After the in situ heat processing, the sample was exposed to ambient conditions for three days. The work function map in fig. 3(c) shows a KPFM measurement after this exposure to ambient conditions. Again the SLG and BLG sheets exhibit *p*-type doping with a work function of 4.82 eV and 4.78 eV, respectively. Thus, the initial values are almost completely restored. We attribute this to the exposure of water and oxygen present in ambient conditions, which causes a large *p*-type doping due to a redox reaction^{10,11}.

To find the origin of the observed contrast inversion in the surface potential, we investigated a sample in ambient conditions using AFM and Raman spectroscopy. In fig. 4(a), an ambient AFM topography of a similar treated - heating to 600°C in UHV - mica supported graphene flake is shown. The few layer part of the graphene flake is covered with nanoblister that are up to 15 nm in height and about 400 nm in diameter. Additionally, round plateau-like structures of similar diameter with a constant height of about 1 nm are observed. These flat plateaus could very well be the remnants of ruptured nanoblister. Shown in fig. 4(b) are the Raman spectra of SLG graphene before (black line) and after (red line) heat processing. In its pristine condition the Raman spectrum consists of the well known first order non resonant *G* mode at 1588 cm⁻¹ and the resonant 2*D* mode at 2645 cm⁻¹. With a full width half maximum (FWHM) of 24 cm⁻¹ for the 2*D* mode, this Raman spectrum can be unambiguously assigned to SLG³³. After heating in UHV two new modes have evolved in the Raman spectrum, the *D* and *D'* mode, which are both induced by disorder³⁴⁻³⁶; in addition the 2*D* mode is suppressed. The presence of the *D* and *D'* mode indicate a very high defect density. Raman spectroscopy can be used to quantify the amount and even the nature of disorder in graphene as well by determining the I_D/I_G and $I_{D'}/I_G$ intensity ratios. Here, we find $I_D/I_G = 1.7$ and $I_{D'}/I_G = 6.3$, respectively. From comparison with published data we estimate that the defects here are mainly vacancy defects³⁷ and the mean distance between defect sites is on the order

of $L_D < 5$ nm^{38,39}. In an attempt to correlate the measured morphology with the defect distribution we used Raman mapping. In fig. 4(c) the *D/G*-peak intensity ratio distribution of the measured sample area can be seen. Due to the very different lateral resolution of the two methods, a one-to-one correlation is not possible. Nevertheless, at many of the locations where large nanoblister and plateaus (most likely ruptured nanoblister) were observed in the AFM image, the Raman map does show areas with an increased *D/G* ratio (marked in fig. 4(c)). This strongly suggests that the formation of nanoblister is accompanied by a significant defect formation in graphene.

Discussion

The experimental evidence presented above suggests that the work function of graphene on mica is governed by different mechanisms which can be controlled by thermal processing. In the following we will discuss three possible mechanisms induced by heat: removal of adsorbates, substrate changes and defect formation.

Any kind of adsorbate is expected to have a large influence on the properties of graphene. For example, graphene field effect transistors of graphene exfoliated on SiO₂ usually show very poor transport characteristics without proper cleaning by e.g. current annealing or annealing in forming gas of the device prior to measurement. Here, we are dealing with different adsorbates, namely water (from the humidity always present in ambient conditions) and air (O₂, N₂, etc.). Their effect on (non-defective) SLG has been investigated by several groups^{9,10,40-42}. Hitherto, only *p*-type doping of graphene on mica has been reported, but all data has been obtained under ambient conditions²⁴, where electrophilic adsorbates can be expected to mask the intrinsic properties of graphene. In general, the adsorbates obviously result in an effective *p*-type doping as confirmed by our data. As we could show, it is basically impossible to completely remove the water from in between graphene and mica, but heating to 600°C ensures that no water is adsorbed on top of graphene and that the intercalated water layer has been successfully removed at least in some areas. From our locally resolved KPFM data, we can easily resolve the difference between areas with the IWL present and areas without the IWL. This enables us to reveal the different and seemingly adverse effects that water may



have on work function measurements: With samples prepared under ambient conditions, intercalated water leads to a decrease of the p -type doping level (see fig. 3(c)), while for heated graphene on mica, intercalated water decreases the number of excess electrons, i.e. lowers the n -type doping level (see fig. 3(b)). These findings clearly underline the importance of UHV measurement when performing quantitative KPFM studies to determine intrinsic properties of graphene.

The second mechanism that may give rise to changes of the work function of graphene is the charge transfer from the substrate. It has been shown that the doping level of graphene is very sensitive to the mica surface configuration⁴³. From our KPFM data we find that the mica substrate does indeed show a change of its work function from 4.6 to 3.4 eV upon heating (see fig. 2), indicating that the mica surface undergoes strong changes towards an electro negative surface. This transition is most likely driven by a depletion of potassium ions on the mica surface⁴³. The fact that we observe a continuous change in the graphene work function upon heating from 5.1 eV (p -type doping) to 3.9 eV (n -type doping), can thus be interpreted in terms of an increasing electron charge transfer from the mica substrate to graphene due to the increasing dehydration of the mica surface.

Apart from direct charge transfer from the mica substrate itself, the heat induced changes of the mica substrate may have an impact on the work function as well. Significant defect formation in graphene can be detected after heating to about 600°C where the dehydration of mica sets in^{44,45}. Based on the observations presented above we therefore suggest that the following mechanism is giving rise to defect formation in graphene: Upon excessive heating mica is dehydrated because the chemically bound water evaporates from within the silicate. This water cannot permeate through the graphene layer and will thus accumulate and form nanoblisters trapping the water molecules. This is corroborated by the fact that graphene nanoblisters are reportedly accompanied by defect formation^{46–49}. In addition, in the process of the dehydration of mica, O₂ is formed and thus oxidative etching as observed by Yamamoto et al. of graphene on mica may play a role for the defect creation formation as well^{45,50}.

In summary, we have shown that for mica supported graphene heating in UHV to temperatures of 600°C is no feasible way to free graphene of interfacial water layers which are confined during sample preparation in ambient. The thermal processing of mica in UHV causes the formation of nanoblisters in the graphene sheet. These structural features are the origin of a very high defect density present in graphene after heating. Kelvin probe measurements reveal, that while pristine graphene flakes on mica show p -type doping behaviour, defective graphene on dehydrated mica is heavily n -type doped. This transition is observed for bilayer graphene on mica as well. The exposure of defective graphene to ambient conditions causes again a transition from n -type back to p -type characteristic for pristine graphene on mica. By a detailed analysis of our data we could unravel the interplay of different mechanisms contributing to the charge carrier transfer to and from graphene.

We would like to conclude by pointing out that our findings are not limited to the case of graphene on mica but have more general implications. From the data presented above it is evident that Kelvin probe force microscopy, Raman spectroscopy and even transport measurements performed in ambient conditions are not suitable to probe the intrinsic properties of graphene. These can only be accessed under the well-defined conditions in ultra high vacuum.

Methods

Sample preparation. Graphene was exfoliated a HOPG crystal (Momentive Performance Materials - USA) in ambient (room humidity typically 40%) onto a freshly cleaved muscovite mica substrate (MaTeck - Germany). Single layer graphene flakes were located using optical microscopy and unambiguously identified with Raman spectroscopy using a Horiba Labram ($\lambda = 633$ nm, $P < 1$ mW).

Ambient characterization. Atomic force microscopy measurements in ambient have been performed using a Veeco Dimension 3100 system and Nanosensors NCHR cantilevers ($f_0 \approx 300$ kHz). For the Raman mappings a Renishaw InVia Raman spectrometer has been used. The step width has been set to 100 nm, the spotsize of the laserbeam is below 1 μm ($\lambda = 532$ nm, $P = 0.4$ mW).

UHV characterization. In situ NC-AFM measurements ($p_b = 1 \times 10^{-10}$ mbar) were conducted using a RHK UHV 7500 system and the PLL Pro 2 controller. Highly conducting Si cantilevers (Vistaprobe T300) with typical resonant frequencies of $f \approx 300$ kHz are used for in situ AFM. Kelvin probe force microscopy⁵¹ was performed by applying an AC voltage of $U_{AC} \approx 1$ V and $f_{AC} \approx 1$ kHz. The built in lock-in amplifier of the PLL Pro2 controller is used to apply a DC voltage in order to minimize the resulting electrostatic force caused by the contact potential difference between the tip and surface. During the heating the temperature of the samples was monitored using a thermocouple.

- Novoselov, K. S. *et al.* Two-dimensional gas of massless dirac fermions in graphene. *Nature* **438**, 197–200 (2005).
- Kim, Y. *et al.* Breakdown of the Interlayer Coherence in Twisted Bilayer Graphene. *Phys. Rev. Lett.* **110**, 096602 (2013).
- Schedin, F. *et al.* Detection of individual gas molecules adsorbed on graphene. *Nature Mat.* **6**(9), 652–655 (2007).
- Balandin, A. A. *et al.* Superior thermal conductivity of single-layer graphene. *Nano Lett.* **8**, 902–907 (2008).
- Lee, C., Wei, X., Kysar, J. W. & Hone, J. Measurement of the elastic properties and intrinsic strength of monolayer graphene. *Science* **321**, 385–388 (2008).
- Xia, F., Mueller, T., Lin, Y.-M., Valdes-Garcia, A. & Avouris, P. Ultrafast graphene photodetector. *Nat. Nanotech.* **4**, 839–843 (2009).
- Messina, R. & Ben-Abdallah, P. Graphene-based photovoltaic cells for near-field thermal energy conversion. *Sci. Rep.* **3**, (2013).
- Cohen-Tanugi, D. & Grossman, J. C. Water desalination across nanoporous graphene. *Nano Lett.* **12**, 3602–3608 (2012).
- Wehling, T. O., Lichtenstein, A. I. & Katsnelson, M. I. First-principles studies of water adsorption on graphene: The role of the substrate. *Appl. Phys. Lett.* **93**, 202110 (2008).
- Ryu, S. *et al.* Atmospheric oxygen binding and hole doping in deformed graphene on a sio 2 substrate. *Nano Lett.* **10**, 4944–4951 (2010).
- Levesque, P. L. *et al.* Probing charge transfer at surfaces using graphene transistors. *Nano Lett.* **11**(1), 132–137 (2011).
- Kazakova, O., Burnett, T. L., Patten, J., Yang, L. & Yakimova, R. Epitaxial graphene on sic(0 0 0)bar {1 1}§: functional electrical microscopy studies and effect of atmosphere. *Nanotechnology* **24**, 215702 (2013).
- Wang, Y. Y. *et al.* Raman studies of monolayer graphene: The substrate effect. *J. Phys. Chem. C* **112**, 10637–10640 (2008).
- Wang, R. *et al.* Control of carrier type and density in exfoliated graphene by interface engineering. *ACS Nano* **5**, 408–412 (2011).
- Bukowska, H. *et al.* Raman spectra of graphene exfoliated on insulating crystalline substrates. *NJP* **13**, 063018 (2011).
- Chen, J. H. *et al.* Charged-impurity scattering in graphene. *Nature Phys.* **4**, 377–381 (2008).
- Fan, X., Nouchi, R. & Tanigaki, K. Effect of charge puddles and ripples on the chemical reactivity of single layer graphene supported by sio 2/si substrate. *J. Phys. Chem. C* **115**, 12960–12964 (2011).
- Castellanos-Gomez, A. *et al.* Atomically thin mica flakes and their application as ultrathin insulating substrates for graphene. *Small* **7**, 2491–2497 (2011).
- Lippert, G. *et al.* Molecular beam growth of micrometer-size graphene on mica. *Carbon* **52**, 40–48 (2013).
- Lui, C.-H., Liu, L., Mak, K. F., Flynn, G. F. & Heinz, T. F. Ultraflat graphene. *Nature* **462**, 339–341 (2009).
- He, K. T., Wood, J. D., Doidge, G. D., Pop, E. & Lyding, J. W. Scanning tunneling microscopy study and nanomanipulation of graphene-coated water on mica. *Nano Letters* **12**, 2665–2672 (2012).
- Severin, N., Lange, P., Sokolov, I. M. & Rabe, J. P. Reversible dewetting of a molecularly thin fluid water film in a soft graphene–mica slit pore. *Nano Lett.* **12**, 774–779 (2012).
- Goncher, S.-J., Zhao, L., Pasupathy, A. N. & Flynn, G. W. Substrate level control of the local doping in graphene. *Nano Lett.* **12**, 1386–1392 (2013).
- Shim, J. *et al.* Water-gated charge doping of graphene induced by mica substrates. *Nano Lett.* **12**, 648–654 (2012).
- Kim, Y. *et al.* Breakdown of the interlayer coherence in twisted bilayer graphene. *Phys. Rev. Lett.* **12**, 096602 (2013).
- Tiberj, A. *et al.* Reversible optical doping of graphene. *Sci. Rep.* **3**, 2355 (2013).
- Kim, K. S. *et al.* Between scylla and charybdis: Hydrophobic graphene-guided water diffusion on hydrophilic substrates. *Sci. Rep.* **3**, 2309 (2013).
- Xu, K., Cao, P. & Heath, J. R. Graphene visualizes the first water adlayers on mica at ambient conditions. *Science* **329**, 1188–1191 (2010).
- Kleine Bußmann, B., Ochedowski, O. & Schleberger, M. Doping of graphene exfoliated on SrTiO₃. *Nanotechnology* **22**, 265703 (2011).
- Ziegler, D. *et al.* Variations in the work function of doped single- and few-layer graphene assessed by kelvin probe force microscopy and density functional theory. *Phys. Rev. B* **83**, 235434 (2011).



31. Yu, Y.-J. *et al.* Tuning the graphene work function by electric field effect. *Nano Lett.* **9**, 3430–3434 (2009).
32. Panchal, V., Pearce, R., Yakimova, R., Tzalenchuk, A. & Kazakova, O. Standardization of surface potential measurements of graphene domains. *Sci. Rep.* **3**, 2597 (2013).
33. Ferrari, A. C. *et al.* Raman spectrum of graphene and graphene layers. *Phys. Rev. Lett.*, **97**, 187401 (2006).
34. Maultzech, J., Reich, S. & Thomsen, C. Double-resonant raman scattering in graphite: Interference effects, selection rules, and phonon dispersion. *Phys. Rev. B* **70**, 155403 (2004).
35. Thomsen, C. & Reich, S. Double resonant raman scattering in graphite. *Phys. Rev. Lett.* **85**, 5214–5217 (2000).
36. Pimenta, M. A. *et al.* Studying disorder in graphite-based systems by raman spectroscopy. *PCCP* **9**, 1276 (2007).
37. Eckmann, A. *et al.* Probing the nature of defects in graphene by raman spectroscopy. *Nano Lett.* **12**, 3925–3930 (2012).
38. Lucchese, M. M. *et al.* Quantifying ion-induced defects and raman relaxation length in graphene. *Carbon* **48**, 1592–1597 (2010).
39. Cancado, L. G. *et al.* Quantifying defects in graphene via raman spectroscopy at different excitation energies. *Nano Lett.* **11**, 3190–3196 (2011).
40. Sabio, J. *et al.* Electrostatic interactions between graphene layers and their environment. *Phys. Rev. B* **77**, 195409 (2008).
41. Javari, F. *et al.* Tunable bandgap in graphene by the controlled adsorption of water molecules. *Small* **6**, 2535–2538 (2010).
42. Cao, P., Varghese, J. O., Xu, K. & Heath, J. R. Visualizing local doping effects of individual water clusters on gold(111)-supported graphene. *Nano Lett.* **12**, 1459–1463 (2012).
43. Rudenko, A. N., Keil, F. J., Katsnelson, M. I. & Lichtenstein, A. I. Graphene adhesion on mica: Role of surface morphology. *Phys. Rev. B* **83**, 045409 (2011).
44. Cartz, L. & Tooper, B. Dehydration of phlogopite micas studied by high-temperature transmission electron microscopy. *JAP* **36**, 2783 (1965).
45. Wirth, R. Dehydration of mica (phengite) by electron bombardment in a transmission electron microscope (tem). *J. Mater. Sci.* **4**, 327–330 (1985).
46. Lusk, M. & Carr, L. Nanoengineering defect structures on graphene. *Phys. Rev. Lett.* **100**, 175503 (2008).
47. Goler, S. *et al.* Self-assembly and electron-beam-induced direct etching of suspended graphene nanostructures. *JAP* **110**, 064308 (2011).
48. Lu, J., Castro, A., Neto, H. & Loh, K. P. Transforming moiré blisters into geometric graphene nano-bubbles. *Nature Comm.* **3**, 823 (2012).
49. Xuan Lim, C. H. Y. *et al.* A hydrothermal anvil made of graphene nanobubbles on diamond. *Nature Comm.* **4**, 1556 (2013).
50. Yamamoto, M., Einstein, T. L., Fuhrer, M. S. & Cullen, W. G. Charge inhomogeneity determines oxidative reactivity of graphene on substrates. *ACS Nano* **6**, 8335–8341 (2012).
51. Nonnenmacher, M., O’Boyle, M. P. & Wickramasinghe, H. K. Kelvin probe force microscopy. *Appl. Phys. Lett.* **58**, 2921 (1991).
52. Hong, J., Park, M. K., Lee, E. J., Lee, D., Hwang, D. S. & Ryu, S. Origin of New Broad Raman D and G Peaks in Annealed Graphene. *Sci. Rep.* **3**, 2700 (2013).
53. Ishigami, M., Chen, J. H., Cullen, W. G., Fuhrer, M. S. & Williams, E. D. Atomic Structure of Graphene on SiO₂. *Nano. Lett.* **7**, 1643–1648 (2007).

Acknowledgments

This work has been supported by the German Science Foundation (SPP 1459: Graphene and SFB 616: Energy dissipation at surfaces).

Author contributions

O.O. performed the experiment. B.K.B. assisted at NC-AFM imaging. The manuscript was written by O.O. and M.S. All authors reviewed the manuscript.

Additional information

Supplementary information accompanies this paper at <http://www.nature.com/scientificreports>

Competing financial interests: The authors declare no competing financial interests.

How to cite this article: Ochedowski, O., Bussmann, B.K. & Schleberger, M. Graphene on Mica - Intercalated Water Trapped for Life. *Sci. Rep.* **4**, 6003; DOI:10.1038/srep06003 (2014).



This work is licensed under a Creative Commons Attribution-NonCommercial-ShareAlike 4.0 International License. The images or other third party material in this article are included in the article’s Creative Commons license, unless indicated otherwise in the credit line; if the material is not included under the Creative Commons license, users will need to obtain permission from the license holder in order to reproduce the material. To view a copy of this license, visit <http://creativecommons.org/licenses/by-nc-sa/4.0/>